

Printable CsPbI₃ Perovskite Solar Cells with PCE of 19% via an Additive Strategy

Xiaoming Chang, Junjie Fang, Yuanyuan Fan, Tao Luo, Hang Su, Yalan Zhang, Jing Lu, Leonidas Tsetseris, Thomas D. Anthopoulos,* Shengzhong (Frank) Liu,* and Kui Zhao*

All-inorganic CsPbI₃ holds promise for efficient tandem solar cells, but reported fabrication techniques are not transferrable to scalable manufacturing methods. Herein, printable CsPbI₃ solar cells are reported, in which the charge transporting layers and photoactive layer are deposited by fast blade-coating at a low temperature (≤ 100 °C) in ambient conditions. High-quality CsPbI₃ films are grown via introducing a low concentration of the multifunctional molecular additive Zn(C₆F₅)₂, which reconciles the conflict between air-flow-assisted fast drying and low-quality film including energy misalignment and trap formation. Material analysis reveals a preferential accumulation of the additive close to the perovskite/SnO₂ interface and strong chemisorption on the perovskite surface, which leads to the formation of energy gradients and suppressed trap formation within the perovskite film, as well as a 150 meV improvement of the energetic alignment at the perovskite/SnO₂ interface. The combined benefits translate into significant enhancement of the power conversion efficiency to 19% for printable solar cells. The devices without encapsulation degrade only by $\approx 2\%$ after 700 h in air conditions.

X. Chang, J. Fang, Y. Fan, T. Luo, H. Su, Y. Zhang, J. Lu,
 Prof. S. (F.) Liu, Prof. K. Zhao
 Key Laboratory of Applied Surface and Colloid Chemistry
 Ministry of Education
 Shaanxi Key Laboratory for Advanced Energy Devices
 Shaanxi Engineering Lab for Advanced Energy Technology
 School of Materials Science and Engineering
 Shaanxi Normal University
 Xi'an 710119, China
 E-mail: zhaok@snnu.edu.cn
 H. Su, Prof. S. (F.) Liu
 Dalian National Laboratory for Clean Energy
 iChEM
 Dalian Institute of Chemical Physics
 Chinese Academy of Sciences
 Dalian 116023, China
 E-mail: szliu@dicp.ac.cn
 Prof. L. Tsetseris
 Department of Physics
 National Technical University of Athens
 Athens GR-15780, Greece
 Prof. T. D. Anthopoulos
 King Abdullah University of Science and Technology (KAUST)
 KAUST Solar Center (KSC) and Physical Science
 and Engineering Division (PSE)
 Thuwal 23955-6900, Saudi Arabia
 E-mail: thomas.anthopoulos@kaust.edu.sa

 The ORCID identification number(s) for the author(s) of this article can be found under <https://doi.org/10.1002/adma.202001243>.

DOI: 10.1002/adma.202001243

Perovskite semiconductors have emerged as exciting new materials for solar cells due to their unique combination of strong light absorption^[1] and superb charge carrier mobility.^[2] Power conversion efficiencies (PCEs) of perovskite solar cells (PSCs) have risen from 3.8% to a certified 25.2%,^[3–6] which already rival those of other thin-film photovoltaic (PV) devices. One significant advantage of perovskite materials is their ability to be solution-processed at low temperature, which makes perovskite solar cells promising candidates for a high-performance, scalable and low-cost vacuum-free PV technology. Such fast and scalable fabrication paradigms are becoming important for fulfilling the anticipated rapid expansion of PV manufacturing from the annual PV installation of 99.1 gigawatt (GW) in 2017^[7,8] to the targeted 1780 GW in 2050.^[9]

Ambient scalable fabrication techniques, such as blade-coating, which facilitate easy entry into mature industrial processes, were first explored for methylammonium (MA) based organic-inorganic perovskite solar cells.^[10,11] Based on detailed understanding of the phase transitions from disordered sol-gel to solvated intermediate and final perovskites,^[12–15] the growth can be well-controlled for a smooth and highly crystalline film with suppressed charge trap concentration. As a result, the PCE of organic-inorganic perovskite solar cells based on ambient blade-coating recently increased to 21.9% for an 8 mm² single cell.^[16] Unfortunately, MA-based perovskite solar cells suffer from poor thermal stability because of the volatile MA⁺ cation. Replacing MA⁺ with Cs⁺ cations (e.g., CsPbI₃) has allowed for significantly improved thermal stability and a slight increase of the bandgap (≈ 1.7 eV), which together hold promise for efficient tandem solar cells.^[17–22]

However, from a materials point of view, all-inorganic CsPbI₃ perovskite tends to form a thermodynamically stable δ -phase instead of the optically active black phases (α , β , γ) at operating temperature of solar cells.^[23–26] Importantly, the phase degradation of active black phases is accelerated in ambient conditions due to its sensitivity to moisture. For these reasons, all high-performance CsPbI₃ solar cells reported to date—without exception—have been fabricated in an inert atmosphere via spin-coating.^[21,23,27] Recent findings showed that a more stable β -CsPbI₃ than other black phases can be deposited at a low temperature in an inert atmosphere.^[21,23] However, our previous

observation indicated that, in the case of ambient scalable fabrication of all-inorganic perovskite (e.g., CsPbI_2Br) solar cells, a slow drying process during low-temperature deposition allows for moisture attack, which suppresses crystallization of the precursors.^[13] Such unwanted moisture attack to perovskite films can in principle be suppressed during fast ambient crystallization processes such as those used for scalable manufacturing. However, from a thermodynamics point of view, the fast crystallization generally results in poor film formation and high trap concentrations, which in turn decrease both the efficiency and operating stability of solar cells. Therefore, to realize ambient scalable fabrication of high-performance CsPbI_3 solar cells, it is critically important to reconcile the conflict between fast deposition and film quality including energy misalignment and trap formation.

Here, we report high-performance printable CsPbI_3 solar cells realized via blade-coating SnO_2 , CsPbI_3 , and spiro-OMeTAD layers at $\leq 100^\circ\text{C}$ in ambient conditions. Airflow introduced straight after the blade helps to accelerate evaporation of the CsPbI_3 ink and suppress moisture attack during crystal nucleation and growth. The molecular additive $\text{Zn}(\text{C}_6\text{F}_5)_2$ ^[28] at a low concentration level of 0.04 mmol L^{-1} was introduced into perovskite solution to improve optoelectronic properties of the blade-coated CsPbI_3 film. The location of $\text{Zn}(\text{C}_6\text{F}_5)_2$ and

its interaction with perovskite, were investigated using time-of-flight secondary-ion mass spectroscopy (TOF-SIMS), optical absorption spectroscopy, X-ray diffraction (XRD) measurements, and theoretical calculations. The results show that the presence of $\text{Zn}(\text{C}_6\text{F}_5)_2$ does not influence the crystal structure and crystallite size of CsPbI_3 , but chemisorbs on perovskite surface, leading to the formation of energy gradients within the perovskite layer and an improved energy band alignment at the perovskite/ SnO_2 interface. Additionally, $\text{Zn}(\text{C}_6\text{F}_5)_2$ suppresses trap formation within the perovskite film fabricated in ambient air. The combined effects result to printable CsPbI_3 solar cells with PCE = 19%, which is significantly higher than control pristine cells (16.97%), primarily due to improvements in the open-circuit voltage (V_{oc}) and fill factor (FF).

Printable CsPbI_3 solar cells were realized via blade-coating in ambient air with the relative humidity (RH) at $\approx 35\%$ (Figure 1a). Films of SnO_2 , CsPbI_3 , and spiro-OMeTAD were blade-coated at $\leq 100^\circ\text{C}$ substrates and used as the electron transporting layer, photoactive layer, and hole transporting layer, respectively. Landau-Levich flow is created when the blade spreads the precursor solution with a high speed of 1.5 m min^{-1} . Airflow was introduced right after the blade to accelerate evaporation of the ink. This enables scalable fabrication of smooth and uniform films of SnO_2 , CsPbI_3 , and spiro-OMeTAD. To tune the

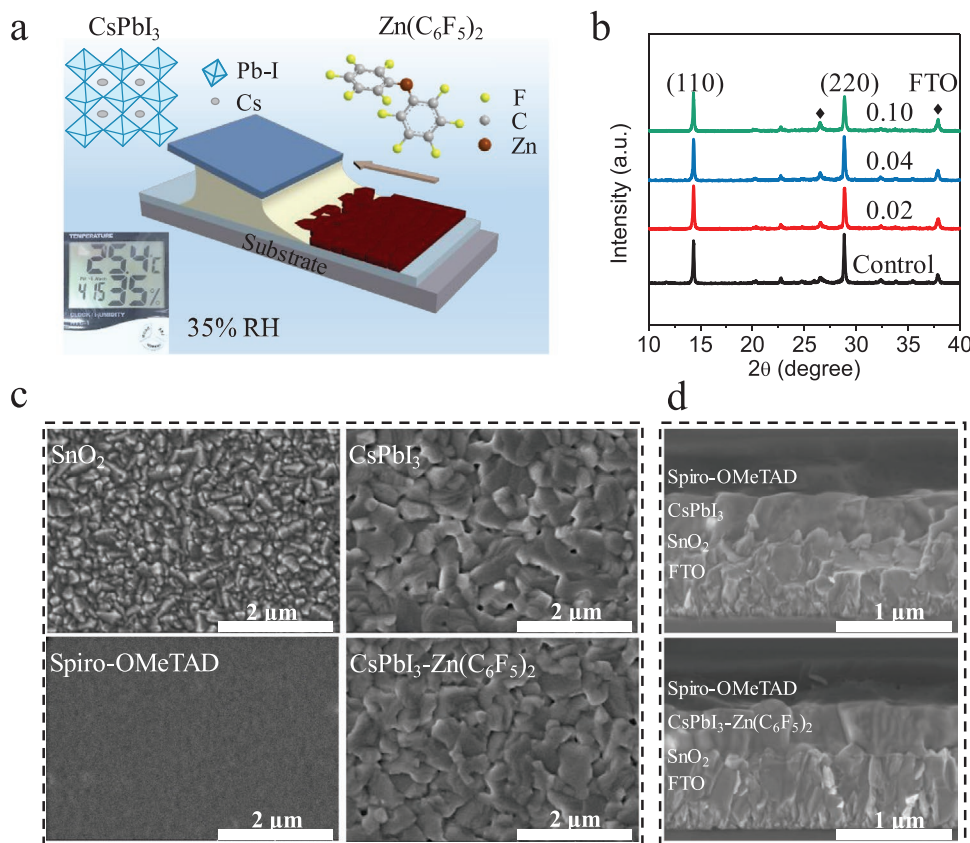


Figure 1. Scalable ambient fabrication. a) Schematic of blade-coating for the SnO_2 , CsPbI_3 perovskite, and Spiro-OMeTAD layers. The ambient humidity is $\approx 35\%$ RH. Room temperature is $\approx 25^\circ\text{C}$. The substrate temperature ranges from 25 to 100°C . The $\text{Zn}(\text{C}_6\text{F}_5)_2$ is introduced into CsPbI_3 as an additive. b) XRD patterns of the neat CsPbI_3 (control) films and the CsPbI_3 films treated with different concentration (mmol L^{-1}) of $\text{Zn}(\text{C}_6\text{F}_5)_2$ additive. c) Top-view SEM images of the blade-coated SnO_2 , Spiro-OMeTAD, neat CsPbI_3 and $\text{CsPbI}_3\text{-Zn}(\text{C}_6\text{F}_5)_2$ films. d) Cross-section SEM image of the blade-coated neat CsPbI_3 and $\text{CsPbI}_3\text{-Zn}(\text{C}_6\text{F}_5)_2$ films.

Table 1. The PV performance statistics of the CsPbI₃ and CsPbI₃-Zn(C₆F₅)₂ based PSCs (39 devices).

Sample		V _{oc} [V]	J _{sc} [mA cm ⁻²]	FF [%]	PCE [%]
CsPbI ₃	average	1.05 ± 0.02	19.29 ± 0.54	77.39 ± 2.00	15.74 ± 0.66
	max	1.07	19.87	79.63	16.97
CsPbI ₃ -Zn(C ₆ F ₅) ₂	average	1.10 ± 0.02	20.21 ± 0.42	80.94 ± 0.65	18.00 ± 0.47
	max	1.12	20.67	81.98	19.00

optoelectronic properties of the CsPbI₃ film, a low concentration of fluoride-containing Lewis acid material Zn(C₆F₅)₂ was introduced as an additive. It has recently been shown that addition of minute amount of Zn(C₆F₅)₂ in organic semiconducting blends plays a dual role, first acting as a p-dopant, and second as a microstructure modifier due to its ability to control the crystallization dynamics of the small-molecule component present in the blend.^[28]

We first evaluated the crystal structure of the CsPbI₃ films due to its critical effect on optoelectronic properties. For this purpose the blade-coated CsPbI₃ films were treated with thermal annealing in ambient conditions at 180°C for 20 min. The XRD analysis shows two main diffraction peaks at $2\theta = 14.2^\circ$ and 28.6° , which can be indexed to the (110) and (220) reflections of the β -CsPbI₃ (P4/mmb) phase (Figure 1b). These are consistent with recent reports^[23,29] and indicates a preferred orientation in the (110) direction (Figure S1, Supporting Information). We note that the often-observed diffraction peaks at 9.9° , 13.2° , and 22.8° assigned to the orthorhombic (Pnma) yellow δ -phase^[30] are completely absent suggesting the phase pure β -CsPbI₃ films. On the other hand, the Zn(C₆F₅)₂-containing CsPbI₃ films, hereafter abbreviated as CsPbI₃-Zn(C₆F₅)₂, exhibit almost identical diffraction pattern with the control (i.e., pristine CsPbI₃) layer. Increasing Zn(C₆F₅)₂ concentration from 0 to 0.02, 0.04, and 0.10 mmol L⁻¹ does not lead to noticeable variations in the peak position and crystal orientation. This indicates that the Zn(C₆F₅)₂ treatment does not alter the CsPbI₃ crystal structure. The full width at half maxima values of the diffraction peak (220) for all CsPbI₃ films show a negligible variation in the range of ≈ 0.15 – 0.18° , indicating almost identical crystal size irrespective of the additive treatment. In short, we demonstrated β -CsPbI₃ film growth via an ambient scalable deposition method. Addition of low concentrations of Zn(C₆F₅)₂ does not affect the CsPbI₃ crystal structure and size.

Next, we investigated the morphology of blade-coated layers of SnO₂, CsPbI₃, and Spiro-OMeTAD. Scanning electron microscopy (SEM) analysis reveals a compact surface for the SnO₂ layer with 20- to 300-nm-sized grains (Figure 1c). The Spiro-OMeTAD film is uniform without noticeable blemishes or pinholes. High uniformity with densely packed submicron-sized grains was observed for both the control CsPbI₃ and the CsPbI₃-Zn(C₆F₅)₂ films. Addition of Zn(C₆F₅)₂ did not change the grain size and uniformity of the CsPbI₃ film, in agreement with the XRD results. Figure 1d shows the cross-sectional SEM images of a complete device based on SnO₂, CsPbI₃, and spiro-OMeTAD layers. The layer thickness of SnO₂, CsPbI₃, and spiro-OMeTAD are ≈ 30 , 400–450, and ≈ 700 nm, respectively. The CsPbI₃ grains appear well connected in both pristine CsPbI₃ and CsPbI₃-Zn(C₆F₅)₂ films, without noticeable difference on grain packing. Again, these observations indicate that

incorporation of Zn(C₆F₅)₂ is unable to change the morphology of CsPbI₃ films via ambient blade-coating.

Printable solar cells were constructed with the planar device configuration of FTO/SnO₂/Perovskite/Spiro-OMeTAD/Au. The active cell area is 0.09 cm² and the device was measured under ambient conditions (humidity of $\approx 40\%$ RH, room temperature of 25°C). The average PCE (PCE_{ave}) for the control CsPbI₃ cell is 15.74(± 0.66)% (Table 1 and Figure 2a). The PCE_{ave} values increase to a peak of 18.00(± 0.47)% for devices treated with 0.04 mmol L⁻¹ Zn(C₆F₅)₂. Increasing the additive concentration further leads to a decline in cell efficiency (Figure S2, Supporting Information). The PCE histogram for optimized CsPbI₃-Zn(C₆F₅)₂ cells exhibits a narrow PCE distribution suggesting improved reproducibility (Figure 2a), which is particularly important for scalable manufacturing. The significantly enhanced PCE_{ave} for CsPbI₃-Zn(C₆F₅)₂ solar cells in contrast to the control is ascribed to the sharp increases in V_{oc} and FF, along with a slight improvement in short-circuit current (J_{sc}). For example, the V_{oc} increases prominently from 1.05(± 0.02) to 1.10(± 0.02) V, along with an increase in the FF from 77.39(± 2.00)% to 80.94(± 1.15)%. However, a slight increase from 19.29(± 0.54) to 20.21(± 0.42) mA cm⁻² is observed in J_{sc}. We achieved the highest PCE of 19.00% for the optimized CsPbI₃-Zn(C₆F₅)₂ devices, with a V_{oc} of 1.12 V, a J_{sc} of 20.67 mA cm⁻², and a FF of 81.98% (Table 1 and Figure 2b). This is on par with the best performance metrics reported to date for CsPbI₃-based solar cells fabricated under inert atmosphere via spin-coating.^[13] This excellent photovoltaic performance highlights the tremendous potential of Zn(C₆F₅)₂ as a functional additive for printable solar cells.

We further conducted operational stability measurements under AM 1.5G one-sun illumination conditions in air (at 25°C, and $\approx 40\%$ RH) (Figure 2c). A stabilized 18.85% output of a champion CsPbI₃-Zn(C₆F₅)₂ cell was obtained within 3 min continuous illumination. Figure S3, Supporting Information shows PCE evolution of the devices without encapsulation in air condition (dark environment, 20% RH, 25°C), which degrades only by $\approx 2\%$ after 700 h. The external quantum efficiency (EQE) shows higher intensity in the range of 500–730 nm for the CsPbI₃-Zn(C₆F₅)₂ as compared to the control cell, hinting to the possibility of higher charge extraction efficiency. The integrated current from the EQE spectra is 20.61 mA cm⁻² for the CsPbI₃-Zn(C₆F₅)₂ cell, which is within the 5% deviation from the measured J_{sc}. The integrated current is slightly higher to that calculated for the control cell (19.16 mA cm⁻²) (Figure 2d), in agreement with the higher J_{sc} measured from the J-V characteristics under simulated illumination.

In order to understand why the addition of a small amount of Zn(C₆F₅)₂ improves the V_{oc} and FF, we carried out a range of complementary characterization measurements. TOF-SIMS

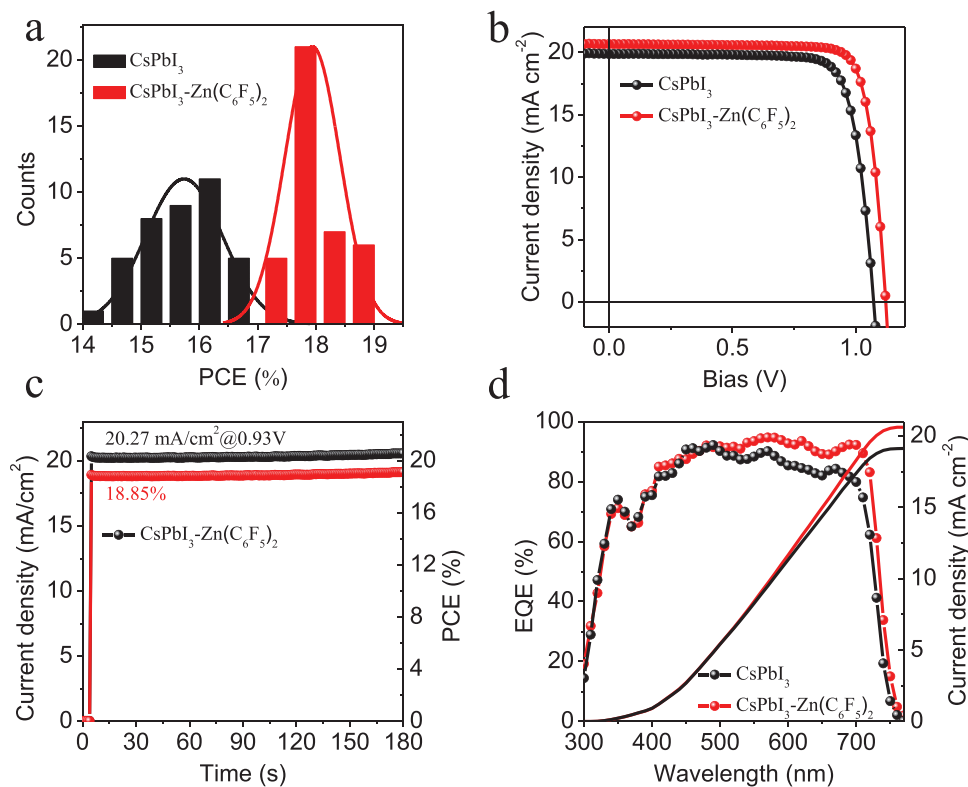


Figure 2. Photovoltaic performance. a) Efficiency histogram of the control CsPbI_3 and the $\text{CsPbI}_3\text{-Zn}(\text{C}_6\text{F}_5)_2$ films based solar cells (effective cell area of 0.09 cm^2 , 39 devices). b) $J\text{-}V$ curves of the champion cell for the control CsPbI_3 and the $\text{CsPbI}_3\text{-Zn}(\text{C}_6\text{F}_5)_2$ based solar cells. c) Stabilized output curves of the champion $\text{CsPbI}_3\text{-Zn}(\text{C}_6\text{F}_5)_2$ -based solar cells. d) The EQE for the control CsPbI_3 and the $\text{CsPbI}_3\text{-Zn}(\text{C}_6\text{F}_5)_2$ -based solar cells.

was first performed to probe the depth profiles of the atomic species throughout the $\text{CsPbI}_3\text{-Zn}(\text{C}_6\text{F}_5)_2$ film on the SnO_2/FTO substrate (Figure 3a). Signals signifying the presence of Zn, C, and F associated with $\text{Zn}(\text{C}_6\text{F}_5)_2$ are not observed in the bulk of the $\text{CsPbI}_3\text{-Zn}(\text{C}_6\text{F}_5)_2$ layers, but do appear close to the perovskite/ SnO_2 interface, where a rapid increase in their intensities is clearly observed along declining signals for Cs, Pb, and I. The 3D reconstructed images of the elemental distribution are displayed in Figure S4, Supporting Information, which highlights the preferential accumulation of $\text{Zn}(\text{C}_6\text{F}_5)_2$ molecules at the bottom of the perovskite layer. X-ray photoelectron spectroscopy analysis on the surface of the pristine CsPbI_3 and the $\text{CsPbI}_3\text{-Zn}(\text{C}_6\text{F}_5)_2$ films indicates a similar elemental distribution, suggesting an absence of $\text{Zn}(\text{C}_6\text{F}_5)_2$ on the perovskite surface (Figure S5, Supporting Information). It can thus be deduced from these measurements that the $\text{Zn}(\text{C}_6\text{F}_5)_2$ additive prefers to accumulate close to the perovskite/ SnO_2 interface, as illustrated in Figure 3b.

We then probe the role of the $\text{Zn}(\text{C}_6\text{F}_5)_2$ at the perovskite/ SnO_2 interface. We first introduced a low concentration of $\text{Zn}(\text{C}_6\text{F}_5)_2$ into PbI_2 solution and found a blue-shift of the absorption (Figure S6a, Supporting Information), which suggests an interaction between the $\text{Zn}(\text{C}_6\text{F}_5)_2$ and the PbI_2 . Further evidences were found that the $\text{PbI}_2\text{-Zn}(\text{C}_6\text{F}_5)_2$ film is optically more transparent than pristine PbI_2 layers of the same thickness. The $\text{PbI}_2\text{-Zn}(\text{C}_6\text{F}_5)_2$ film exhibits significantly lower absorption intensity and crystallinity than the pristine PbI_2 film (Figure S6b-d, Supporting Information). Atomic-scale details

of the interactions between the $\text{Zn}(\text{C}_6\text{F}_5)_2$ and the constituent parts of the perovskite/ SnO_2 interface were further investigated using density functional theory (DFT) calculations. The findings indicate that a $\text{Zn}(\text{C}_6\text{F}_5)_2$ molecule interacts, indeed, strongly, with both the (001) surface of SnO_2 and the (001) surface of $\beta\text{-CsPbI}_3$ (either I-terminated, or Pb-terminated) (Figure 3c-e). For example, the $\text{Zn}(\text{C}_6\text{F}_5)_2$ molecule binds strongly to the surface of SnO_2 by forming two Zn–O bonds with a binding energy of 3.41 eV (Figure 3c). The electronic densities of states show a negligible influence of this chemisorption on electronic properties of the SnO_2 surface. A $\text{Zn}(\text{C}_6\text{F}_5)_2$ molecule also chemisorbs strongly on $\beta\text{-CsPbI}_3$ through Zn–I bonds, with binding energies of 3.35 eV and 3.84 eV for the Pb-terminated and I-terminated CsPbI_3 surfaces (Figure 3d,e, the corresponding Zn–I bond lengths are 2.73 Å and 2.75 Å), respectively. Furthermore, strong F–Cs interaction was found between the $\text{Zn}(\text{C}_6\text{F}_5)_2$ and CsPbI_3 , as confirmed by the relatively short Cs–F distances of 3.10–3.20 Å. These results indicate a strong chemisorption of the $\text{Zn}(\text{C}_6\text{F}_5)_2$ on perovskite and SnO_2 surface.

To gain insight into the role of the strong chemisorption of the $\text{Zn}(\text{C}_6\text{F}_5)_2$ on electronic properties of CsPbI_3 , we performed ultraviolet photoelectron spectroscopy (UPS) on blade-coated films to evaluate the energetic alignment (Figure 3f and Figure S7, Supporting Information). For this purpose we increased the $\text{Zn}(\text{C}_6\text{F}_5)_2$ concentration to 0.40 mmol L^{-1} and decreased the layer thickness to $<50 \text{ nm}$ in order to ensure that the concentration of $\text{Zn}(\text{C}_6\text{F}_5)_2$ on the film's interface

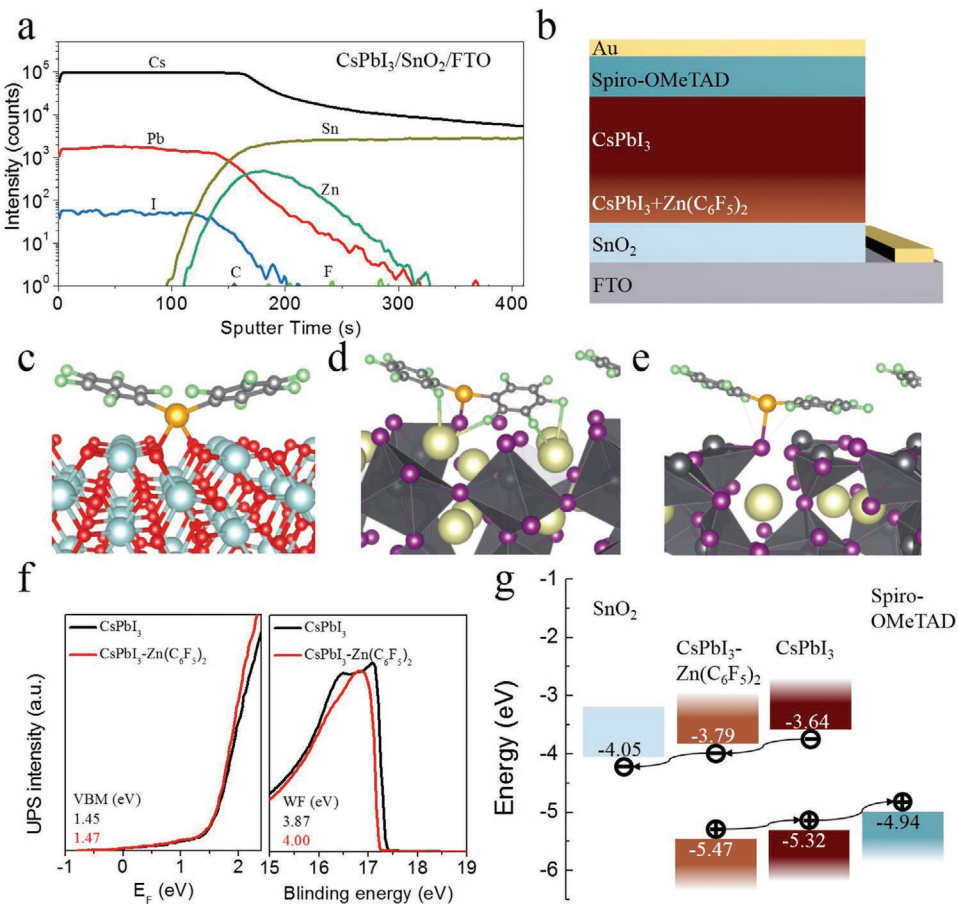


Figure 3. Location of Zn(C₆F₅)₂ and energetic band alignment. a) The characterization of TOF-SIMS for CsPbI₃-Zn(C₆F₅)₂ perovskite sample. b) A scheme showing a preferential accumulation of Zn(C₆F₅)₂ at the CsPbI₃/SnO₂ interface. c) A Zn(C₆F₅)₂ molecule chemisorbed on the (001) surface of SnO₂. d) An I-terminated (001) surface of CsPbI₃. e) A Pb-terminated (001) surface of CsPbI₃ (Sn: light blue, O: red, Cs: light yellow, Pb: dark gray, I: purple, C: gray, F: green, Zn: orange spheres). f) UPS spectra of the CsPbI₃ and CsPbI₃-Zn(C₆F₅)₂ films. g) The energy diagrams of a complete solar cell showing the formation of an energy gradient within CsPbI₃-Zn(C₆F₅)₂ films and a better energetic alignment at the CsPbI₃/SnO₂ interface.

is detectable. Indeed, we observed decreases from -3.64 to -3.79 eV for the conduction band minimum (CBM) and from -5.32 to -5.47 eV for the valence band maximum, respectively, for the CsPbI₃ film with additive treatment. These results indicate that for CsPbI₃-Zn(C₆F₅)₂ films in which the Zn(C₆F₅)₂ molecules accumulate close to the perovskite/SnO₂ interface, an energy gradient exists (Figure 3g). This leads to the formation of a built-in band alignment within the perovskite film, which is beneficial for internal charge separation and charge transfer between the top CsPbI₃ layer and the bottom CsPbI₃-Zn(C₆F₅)₂ layer. Furthermore, the presence of Zn(C₆F₅)₂ improves the energetic alignment of the CBM by 150 meV at the perovskite/SnO₂ interface. In summary, the existence of an energy gradient within the perovskite film and advantageous energetic alignment at the perovskite/SnO₂ interface account for the increased V_{oc} .

Though perovskite vacancies are believed to be shallow electronic traps,^[31] they can form deep traps particularly in layers grown in ambient conditions due to the absorption of water and oxygen at vacancy sites. To ascertain whether the chemisorption influences the formation of vacancies, we studied the trap passivation and charge extraction as both relate to

V_{oc} and FF of the solar cell. We observe a negligible effect of Zn(C₆F₅)₂ on the absorption intensity and the absorbance edge of the CsPbI₃ films (Figure 4a), which remains at ≈ 1.69 eV (≈ 734 nm) (Figure S8, Supporting Information). Surprisingly, addition of Zn(C₆F₅)₂ leads to a sevenfold decrease in the photoluminescence (PL) intensity of the CsPbI₃-Zn(C₆F₅)₂ layer deposited on SnO₂. This suggests a much improved charge transfer at the CsPbI₃-Zn(C₆F₅)₂/SnO₂ interface, which agrees well with the improved energetic alignment at the interface (Figure 3d). Time-resolved PL (TRPL) reveals an important difference in the charge carrier lifetime of the perovskite films (Figure 4b). The lifetime extracted for a CsPbI₃-Zn(C₆F₅)₂ film deposited on glass exhibits is much higher ($\tau_{ave} = 37.6$ ns) than that measured for the control pristine layer ($\tau_{ave} = 3.9$ ns). This significantly increased charge carrier lifetime indicates trap passivation induced by the presence of Zn(C₆F₅)₂ in the CsPbI₃

Further evidence for Zn(C₆F₅)₂-mediated trap passivation were obtained by analyzing the dependence of V_{oc} on the light intensity (Figure 4c). The V_{oc} varies linearly with the light intensity for both the control and CsPbI₃-Zn(C₆F₅)₂ cells. The trap-assisted recombination can be well reflected by the

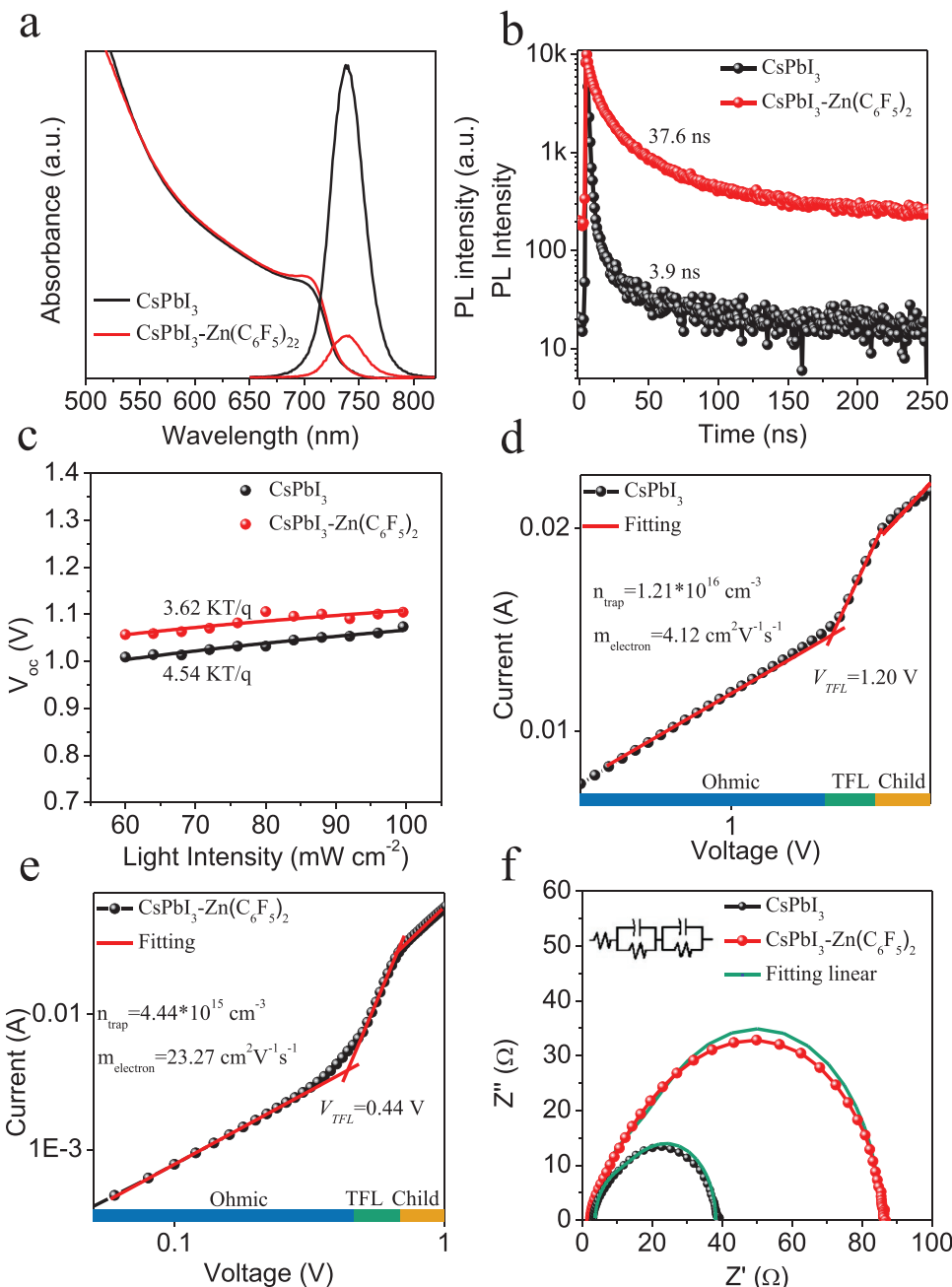


Figure 4. Photophysical properties of CsPbI_3 films. a) Comparison of UV–vis and PL spectra for CsPbI_3 and $\text{CsPbI}_3\text{-Zn}(\text{C}_6\text{F}_5)_2$ films. b) TRPL of perovskite films. c) Open-circuit voltage versus light intensity of CsPbI_3 - and $\text{CsPbI}_3\text{-Zn}(\text{C}_6\text{F}_5)_2$ -based cells. d) Dark I – V measurement of the electron-only device for CsPbI_3 films. e) Dark I – V measurement of the electron-only device for $\text{CsPbI}_3\text{-Zn}(\text{C}_6\text{F}_5)_2$ films. f) Electrical impedance spectroscopy (EIS) of cells based on the CsPbI_3 and $\text{CsPbI}_3\text{-Zn}(\text{C}_6\text{F}_5)_2$ films.

deviation between the slope and the value of (kT/q) (k is the Boltzmann constant, T is temperature, and q is the electric charge). We observed a decrease from 4.54, for the control CsPbI_3 , to 3.62 kT/q for the $\text{CsPbI}_3\text{-Zn}(\text{C}_6\text{F}_5)_2$ cell, suggesting a less pronounced trap-assisted recombination in good agreement with our TRPL data (Figure 4b). Since V_{oc} and FF are related to nonradiative recombination involving traps, the additive-mediated trap passivation should account for the improved V_{oc} and FF in a complete solar cell.

In light of the proposed energetic alignment mechanism, we further explored its effect on the charge carrier mobility. Dark I – V characteristics were measured for electron-only devices comprised of glass/FTO/SnO₂/perovskite/PCBM/Ag (Figure 4d,e). The electron mobility can then be determined using the Mott–Gurney Law.^[32]

$$\mu = \frac{8J_D L^3}{9\varepsilon_0 \varepsilon_r V^2} \quad (1)$$

where, ϵ_0 is the vacuum permittivity, ϵ_r the relative dielectric constant, J_D the current density, L the distance between the electrodes (layer thickness), and V the applied voltage. The trap density, on the other hand, can be determined from the dark I - V characteristics using space-charge-limited current model.^[33]

$$n_{\text{trap}} = \frac{2\epsilon_0\epsilon_r V_{\text{TFL}}}{eL^2} \quad (2)$$

where, V_{TFL} is the onset voltage of the trap-filled limit region, and e is the elementary charge. The electron mobilities were estimated to be 16.26 (± 4.63) and 3.71 (± 0.58) $\text{cm}^2 \text{V}^{-1} \text{s}^{-1}$ for the $\text{CsPbI}_3\text{-Zn(C}_6\text{F}_5)_2$ and the control CsPbI_3 films, respectively. The trap densities determined are $4.72 (\pm 0.68) \times 10^{15}$ and $1.25 (\pm 0.71) \times 10^{16} \text{ cm}^{-3}$ for the $\text{CsPbI}_3\text{-Zn(C}_6\text{F}_5)_2$ and the control CsPbI_3 films, respectively. The remarkably improved electron mobility and decreased trap density agree with UPS and TRPL findings, and indicate that addition of $\text{Zn(C}_6\text{F}_5)_2$ improves the energetic alignment while suppressing the formation of unwanted vacancies.

Interestingly, we also observed an improvement of the recombination resistance at the perovskite/ SnO_2 interface upon $\text{Zn(C}_6\text{F}_5)_2$ addition. Electrical impedance spectroscopy was performed to investigate the values of the recombination resistance (R_{rec}) complete cells comprised of glass/FTO/ SnO_2 /perovskite/spiro-OMeTAD/Au (Figure 4f). Evidently, the R_{rec} values increase significantly from 9.44 to 66.38 Ω upon $\text{Zn(C}_6\text{F}_5)_2$ addition, suggesting reduced charge recombination at the perovskite/ SnO_2 interface. The result is consistent with observations of more efficient electron extraction and the passivation effect (Figure 4a,b).

We reported the development of the first high-performance, printable CsPbI_3 solar cells via ambient blade-coating technique. High quality CsPbI_3 films were realized via a combination of air-flow-assisted drying and the addition of the organic Lewis acid $\text{Zn(C}_6\text{F}_5)_2$. Extensive material and device analysis reveal that the $\text{Zn(C}_6\text{F}_5)_2$ accumulates close to the perovskite/ SnO_2 interface. The strong chemisorption of the $\text{Zn(C}_6\text{F}_5)_2$ at the CsPbI_3 surface leads to the formation of built-in potential, a 150-meV improvement of the energetic alignment at the perovskite/ SnO_2 interface, and suppressed trap formation within perovskite layer. The work highlights the use of functional additives as an effective strategy to reconcile the issues arising from the conflict between fast deposition and film quality, including energy misalignment and trap formation, all particular relevant for ambient scalable manufacturing of perovskite solar cells.

Experimental Section

See experimental details in the Supporting Information.

Supporting Information

Supporting Information is available from the Wiley Online Library or from the author.

Acknowledgements

This work was supported by the National Key Research and Development Program of China (2016YFA0202403, 2017YFA0204800), Key Program project of the National Natural Science Foundation of China (51933010), National Natural Science Foundation of China (61974085), National University Research Fund (GK201802005), the 111 Project (B14041), the National 1000 Talents Plan program (1110010341).

Conflict of Interest

The authors declare no conflict of interest.

Author Contributions

K.Z. designed the project and supervised the work. X.C. performed most of the experiments. J.F. and H.S. helped with the device fabrication. Y.F. helped with the SEM analysis. J.L. helped acquire the TRPL data. T.D.A. and L.T. assisted with the DFT calculation. T.L. and Y.Z. contributed to useful discussions. All authors contributed to the writing and improvement of the manuscript.

Keywords

CsPbI_3 perovskite solar cells, energy alignment, passivation, printable devices

Received: February 21, 2020

Revised: July 13, 2020

Published online: August 31, 2020

- [1] A. Kojima, K. Teshima, Y. Shirai, T. Miyasaka, *J. Am. Chem. Soc.* **2009**, *131*, 6050.
- [2] C. Wehrenfennig, G. E. Eperon, M. B. Johnston, H. J. Snaith, L. M. Herz, *Adv. Mater.* **2014**, *26*, 1584.
- [3] M. M. Lee, J. Teuscher, T. Miyasaka, T. N. Murakami, H. J. Snaith, *Science* **2012**, *338*, 643.
- [4] N. Arora, M. I. Dar, A. Hinderhofer, N. Pellet, F. Schreiber, S. M. Zakeeruddin, M. Grätzel, *Science* **2017**, *358*, 768.
- [5] Q. Jiang, Y. Zhao, X. Zhang, X. Yang, Y. Chen, Z. Chu, Q. Ye, X. Li, Z. Yin, J. You, *Nat. Photonics* **2019**, *13*, 460.
- [6] National Renewable Energy Laboratory (NREL), <https://www.nrel.gov/pv/assets/pdfs/best-research-cell-efficiencies.pdf>, (accessed: August 2019).
- [7] Y. Deng, C. H. Van Brackle, X. Dai, J. Zhao, B. Chen, J. Huang, *Sci. Adv.* **2019**, *5*, eaax7537.
- [8] J. N. Mayer, *Current and Future Cost of Photovoltaics*, Fraunhofer ISE, Freiburg, Germany **2015**.
- [9] M. Schmela, *Global Market Outlook for Solar Power 2018–2022*, SolarPower Europe, Brussels, Belgium **2018**.
- [10] Y. Deng, E. Peng, Y. Shao, Z. Xiao, Q. Dong, J. Huang, *Energy Environ. Sci.* **2015**, *8*, 1544.
- [11] Z. Yang, C. C. Chueh, F. Zuo, J. H. Kim, P. W. Liang, A. K. Y. Jen, *Adv. Energ. Mater.* **2015**, *5*, 1500328.
- [12] J. Li, R. Munir, Y. Fan, T. Niu, Y. Liu, Y. Zhong, Z. Yang, Y. Tian, B. Liu, J. Sun, D.-M. Smilgies, S. Thoroddsen, A. Amassian, K. Zhao, S. Liu, *Joule* **2018**, *2*, 1313.
- [13] Y. Fan, J. Fang, X. Chang, M.-C. Tang, D. Barrit, Z. Xu, Z. Jiang, J. Wen, H. Zhao, T. Niu, D.-M. Smilgies, S. Jin, Z. Liu, E. Q. Li, A. Amassian, S. Liu, K. Zhao, *Joule* **2019**, *3*, 2485.

- [14] J. Li, Y. Liu, X. Ren, Z. Yang, R. Li, H. Su, X. Yang, J. Xu, H. Xu, J.-Y. Hu, A. Amassian, K. Zhao, S. F. Liu, *Adv. Opt. Mater.* **2017**, *5*, 1700102.
- [15] Y. Zhong, R. Munir, J. Li, M.-C. Tang, M. R. Niazi, D.-M. Smilgies, K. Zhao, A. Amassian, *ACS Energ. Lett.* **2018**, *3*, 1078.
- [16] W. Wu, P. N. Rudd, Z. Ni, C. H. Van Brackle, H. Wei, Q. Wang, B. R. Ecker, Y. Gao, J. Huang, *J. Am. Chem. Soc.* **2020**, *142*, 3989.
- [17] A. Swarnkar, A. R. Marshall, E. M. Sanehira, B. D. Chernomordik, D. T. Moore, J. A. Christians, T. Chakrabarti, J. M. Luther, *Science* **2016**, *354*, 92.
- [18] K. Wang, Z. Jin, L. Liang, H. Bian, D. Bai, H. Wang, J. Zhang, Q. Wang, L. Shengzhong, *Nat. Commun.* **2018**, *9*, 4544.
- [19] A. Dutta, S. K. Dutta, S. Das Adhikari, N. Pradhan, *Angew. Chem., Int. Ed.* **2018**, *57*, 9083.
- [20] D. B. Straus, S. Guo, R. J. Cava, *J. Am. Chem. Soc.* **2019**, *141*, 11435.
- [21] Y. Wang, X. Liu, T. Zhang, X. Wang, M. Kan, J. Shi, Y. Zhao, *Angew. Chem., Int. Ed.* **2019**, *58*, 16691.
- [22] J. Shi, Y. Wang, Y. Zhao, *Energy Environ. Mater.* **2019**, *2*, 73.
- [23] Y. Wang, M. I. Dar, L. K. Ono, T. Zhang, M. Kan, Y. Li, L. Zhang, X. Wang, Y. Yang, X. Gao, Y. Qi, M. Grätzel, Y. Zhao, *Science* **2019**, *365*, 591.
- [24] J. A. Steele, H. Jin, I. Dovgaliuk, R. F. Berger, T. Braeckeveldt, H. Yuan, C. Martin, E. Solano, K. Lejaeghere, S. M. J. Rogge, C. Notebaert, W. Vandezande, K. P. F. Janssen, B. Goderis, E. Debroye, Y. Wang, Y. Dong, D. Ma, M. Saidaminov, H. Tan, Z. Lu, V. Dyadkin, D. Chernyshov, V. V. Speybroeck, E. H. Sargent, J. Hofkens, M. B. J. Roeffaers, *Science* **2019**, *365*, 679.
- [25] W. Ke, I. Spanopoulos, C. C. Stoumpos, M. G. Kanatzidis, *Nat. Commun.* **2018**, *9*, 4785.
- [26] H. Zhao, J. Xu, S. Zhou, Z. Li, B. Zhang, X. Xia, X. Liu, S. Dai, J. Yao, *Adv. Funct. Mater.* **2019**, *29*, 1808986.
- [27] Q. Ye, Y. Zhao, S. Mu, F. Ma, F. Gao, Z. Chu, Z. Yin, P. Gao, X. Zhang, J. You, *Adv. Mater.* **2019**, *31*, 1905143.
- [28] A. F. Paterson, L. Tsetseris, R. Li, A. Basu, H. Faber, A. H. Emwas, J. Panidi, Z. Fei, M. R. Niazi, D. H. Anjum, *Adv. Mater.* **2019**, *31*, 1900871.
- [29] A. Marronnier, G. Roma, S. Boyer-Richard, L. Pedesseau, J. M. Jancu, Y. Bonnassieux, C. Katan, C. C. Stoumpos, M. G. Kanatzidis, J. Even, *ACS Nano* **2018**, *12*, 3477.
- [30] G. E. Eperon, G. M. Paternò, R. J. Sutton, A. Zampetti, A. A. Haghhighirad, F. Cacialli, H. J. Snaith, *J. Mater. Chem. A* **2015**, *3*, 19688.
- [31] A. Buin, P. Pietsch, J. Xu, O. Voznyy, A. H. Ip, R. Comin, E. H. Sargent, *Nano Lett.* **2014**, *14*, 6281.
- [32] M. Kiy, P. Losio, I. Biaggio, M. Koehler, A. Tapponnier, P. Günter, *Appl. Phys. Lett.* **2002**, *80*, 1198.
- [33] R. H. Bube, *J. Appl. Phys.* **1962**, *33*, 1733.

Supporting Information

Printable CsPbI₃ Perovskite Solar Cells with PCE of 19% via an Additive Strategy

Xiaoming Chang,¹ Junjie Fang,¹ Yuanyuan Fan,¹ Tao Luo,¹ Hang Su,^{1,2} Yalan Zhang,¹ Jing Lu,¹ Leonidas Tsetseris,³ Thomas D. Anthopoulos,^{4,*} Shengzhong (Frank) Liu,^{1,2,*} Kui Zhao^{1,*}

X. Chang, J. Fang, Y. Fan, T. Luo, H. Su, Y. Zhang, J. Lu, Prof. K. Zhao

¹Key Laboratory of Applied Surface and Colloid Chemistry, Ministry of Education; Shaanxi Key Laboratory for Advanced Energy Devices; Shaanxi Engineering Lab for Advanced Energy Technology, School of Materials Science and Engineering, Shaanxi Normal University, Xi'an 710119, China.

E-mail: zhaok@snnu.edu.cn

H. Su, Prof. S. (F). Liu

²Dalian National Laboratory for Clean Energy; iChEM, Dalian Institute of Chemical Physics, Chinese Academy of Sciences, Dalian, 116023, China.

Email: szliu@dicp.ac.cn

Prof. L. Tsetseris

³Department of Physics, National Technical University of Athens, Athens GR-15780, Greece.

Prof. T. D. Anthopoulos

⁴King Abdullah University of Science and Technology (KAUST), KAUST Solar Center (KSC) and Physical Science and Engineering Division (PSE), Thuwal 23955-6900, Saudi Arabia.

E-mail: thomas.anthopoulos@kaust.edu.sa

Experimental Section

Material preparation: The SnO₂ precursor (Tin (IV) oxide, 15% in H₂O colloidal dispersion) was purchased from Alfa Aesar. *N,N*-dimethylformamide (DMF, 99.8%). Dimethyl sulfoxide (DMSO, 99.9%) was purchased from Sigma-Aldrich. Bis(pentafluorophenyl)zinc (Zn(C₆F₅)₂, 99.7%) was purchased from J&K Scientific Ltd. Cesium iodide (CsI, 99.9%) and HPbI₃ was purchased from p-OLED.

Solution preparation: CsPbI₃ precursor solution: HPbI₃ (0.44 g) and CsI (0.18 g) were dissolved in 1mL (DMF: DMSO = 4:1) and stirred at 25°C in N₂-filled glove box for 12 h. Zn(C₆F₅)₂ was dissolved in DMF and stirred at 25°C in N₂-filled glove box for 20 min. The Zn(C₆F₅)₂ solution was added into the CsPbI₃ precursor solution with concentration of 0.02, 0.04, 0.10 mmol L⁻¹ immediately. The Spiro-OMeTAD solution was consisted of 80 mg Spiro-OMeTAD, 22 μL lithium bis(trifluoromethanesulfonyl) imide solution (520 mg in 1 ml acetonitrile) and 30 μL 4-tert-butylpyridine and 1 mL chlorobenzene. The concentration of SnO₂ solution was decreased by 8-fold prior to usage.

Device Fabrication: The FTO glass (2.9 cm × 2.9 cm) was cleaned using acetone, isopropanol and ethanol and then dried in a N₂ flow before treated by O₃ plasma for 18 min. The key layers of SnO₂, CsPbI₃, and Spiro-OMeTAD were blade-coated at 100°C, 85 °C and 40 °C substrates at a speed of 1.5 m min⁻¹ in ambient conditions. To suppress moisture attack to the CsPbI₃ crystallization, air-flow was introduced after the blade to accelerate drying and crystallization of perovskite ink. The layers of SnO₂ and CsPbI₃ were then treated with thermal annealing at 150°C for 30 min and at 180°C for 20 min respectively.

The device fabrication for the CsPbI₃-Zn(C₆F₅)₂ PSCs is the same with that for the CsPbI₃ PSCs. Finally, 70 nm of gold electrodes on the top of the cell were prepared by thermal evaporation.

Film characterizations

X-ray diffraction (XRD): The crystal structures of perovskite films were characterized using XRD on a Rigaku Smart Lab (X-ray Source: Cu K α , $\lambda = 1.54 \text{ \AA}$).

Scanning electronic morphology (SEM): The surface morphologies of SnO₂, perovskite and Spiro-OMeTAD films were characterized by SEM (FE-SEM; SU-8020, Hitachi).

UV-Vis absorption: Absorption spectra were measured on a PerkinElmer UV-Lambda 950 instrument.

Time-of-flight secondary-ion mass spectroscopy (TOF-SIMS): TOF-SIMS with in situ ion sputtering was used to investigate CsPbI₃-Zn(C₆F₅)₂ perovskite samples by Ion TOF Gmhb5.

Photoluminescence (PL): Steady-state photoluminescence (PL) (excitation at 510 nm, front-side excitation) and time-resolved photoluminescence (TRPL) (excitation at 510 nm, front-side excitation) were measured with a PicoQuant FT-300.

Ultraviolet photoelectron spectroscopy (UPS) and X-ray photoelectron spectroscopy (XPS): UPS and XPS results were acquired on a photoelectron spectrometer (ESCALAB 250Xi, Thermo Fisher Scientific).

Impedance spectroscopic measurements (EIS): EIS were carried out on an electrochemical workstation (IM6ex, Zahner, Germany) with the frequency range from 10 Hz to 4 MHz at open-circuit voltage in the dark conditions.

Density Functional Theory (DFT): DFT calculations were performed with the Perdew-Wang (PW) generalized-gradient approximation (GGA) exchange-correlation (xc) functional,^[1] and projector-augmented waves,^[2] as implemented in the code Quantum Espresso.^[3] Van der Waals interactions were included with the so-called DFT-D2 scheme.^[4] The energy cutoff for the plane wave basis was set at 100 Rydberg and large supercell slabs were used to simulate the surfaces of SnO₂ and β-CsPbI₃ with or without adsorbed molecules. Structures were rendered with the software VESTA.^[5] Due to the large size of the employed supercells, it was not possible to apply post-DFT corrections (e.g. through so-called hybrid xc-functionals) to remedy the well-known underestimation of the energy band gap problem by standard xc-functionals such as the PW-GGA one.

Device characterizations: The J-V performance of the perovskite solar cells was analyzed using a Keithley 2400 SourceMeter under ambient conditions at room temperature, and the illumination intensity was 100 mW cm⁻² (AM 1.5G Oriel solar simulator). The scan range was 3.0 V – -0.1 V, and the bias step was 0.02 V. The power output of the lamp was calibrated using an NREL-traceable KG5-filtered silicon reference cell. The EQE was characterized on a QTest Station 2000ADI system (CrownTech Inc., USA), and the light source was a 300 W xenon lamp. The monochromatic light intensity for the EQE

measurement was calibrated with a reference silicon photodiode. The dark J-V characteristics of the electron-only devices were measured by a Keithley 2400 SourceMeter.

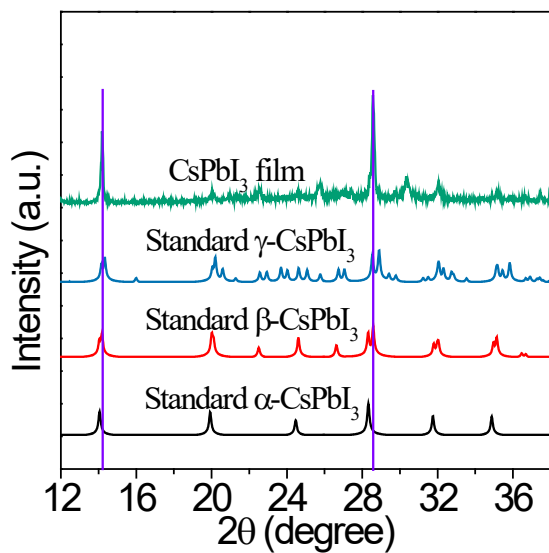


Figure S1. Comparison of XRD patterns of blade-coated CsPbI₃ films on ITO substrate with standard XRD patterns (Marronnier et al (2018)) of α-CsPbI₃, β-CsPbI₃ and γ-CsPbI₃.

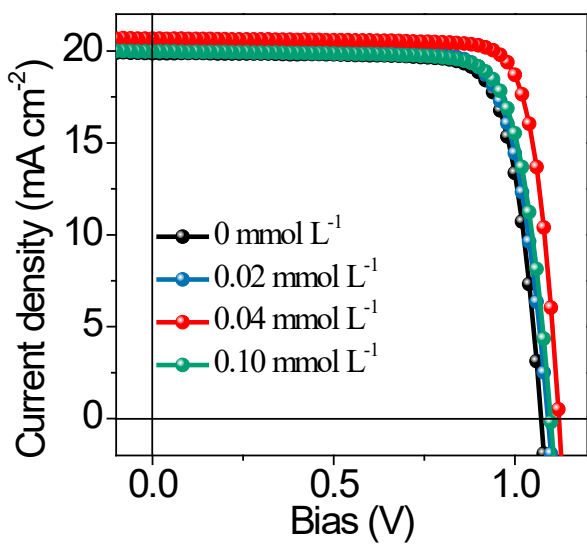


Figure S2. *J-V* curves of the champion CsPbI₃ perovskite solar cells with various Zn(C₆F₅)₂ concentrations.

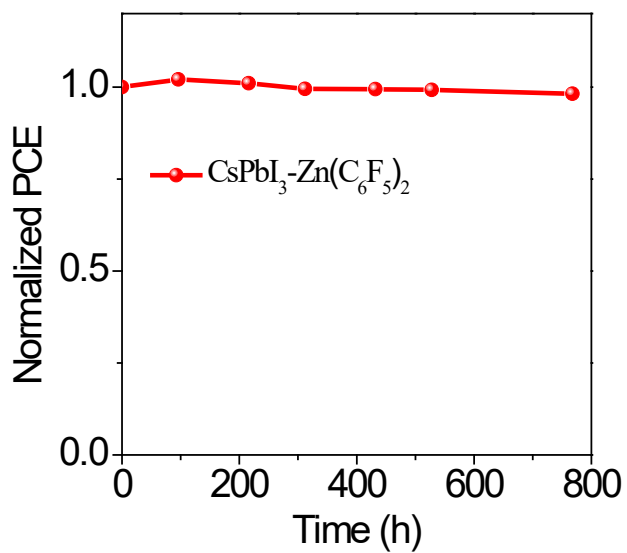


Figure S3. The stability of the non-encapsulated CsPbI₃-Zn(C₆F₅)₂ solar cells exposed to the ambient environment at 20% RH in the dark at room temperature.

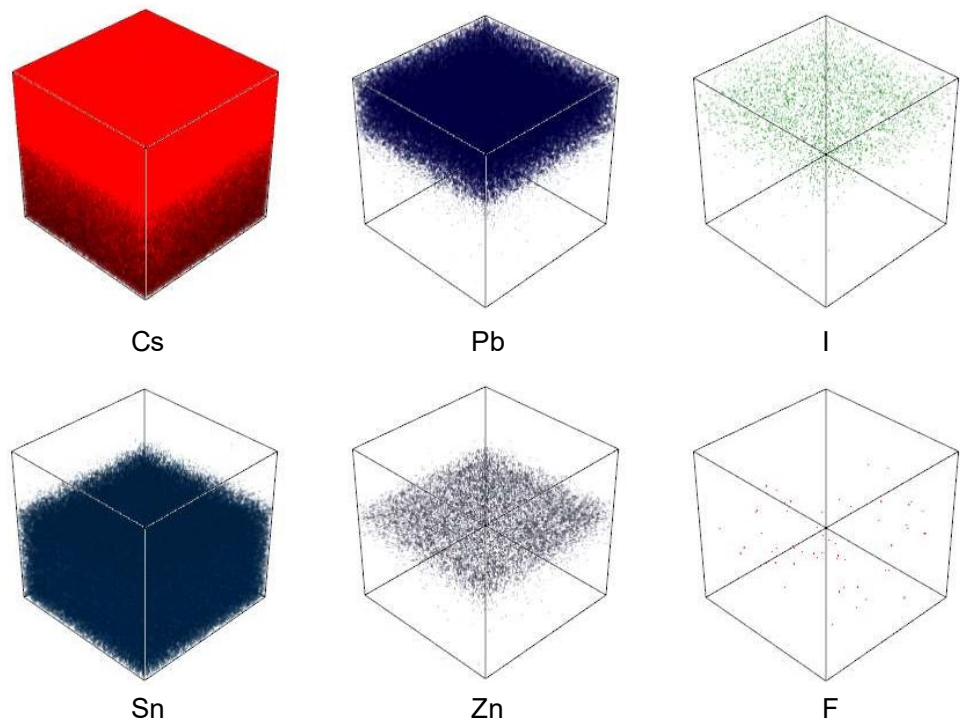


Figure S4. 3D reconstructed images of (a) Cs, (b) Pb, (c) I, (d) Sn, (e) Zn and (f) F in $\text{CsPbI}_3\text{-Zn}(\text{C}_6\text{F}_5)_2$ perovskite film as obtained from the TOF-SIMS analysis.

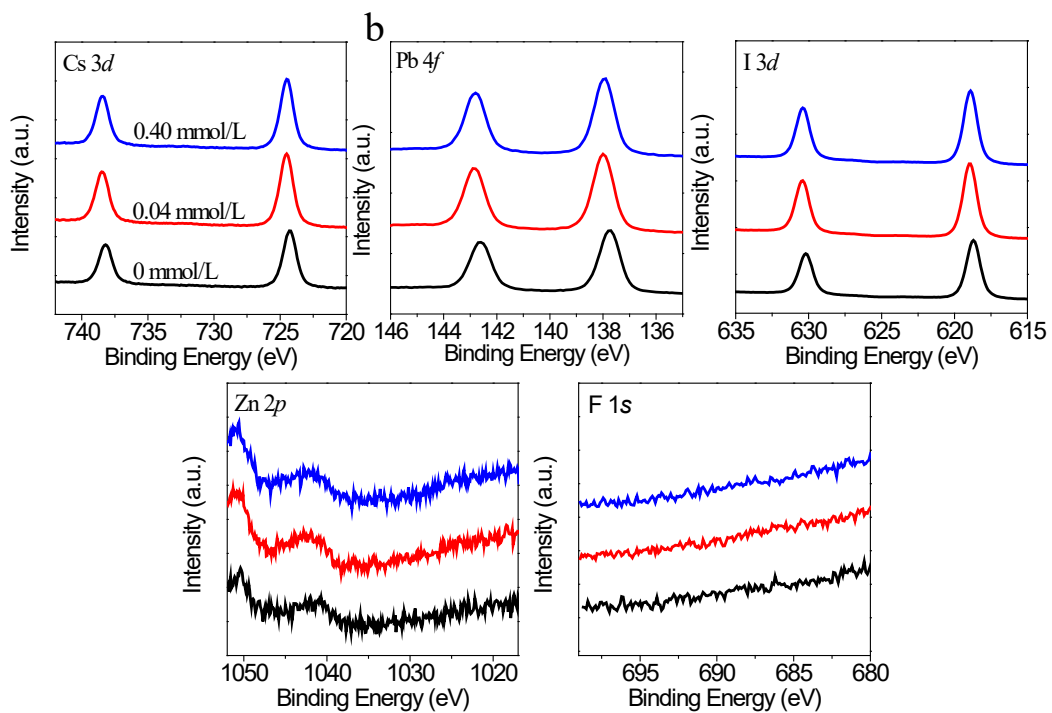


Figure S5. (a) Cs 3d, (b) Pb 4f, (c) I 3d, (d) Zn 2p and (e) F 1s core-level spectra for the CsPbI₃ perovskite films with Zn(C₆F₅)₂ concentrations of 0, 0.04, and 0.40 mmol L⁻¹.

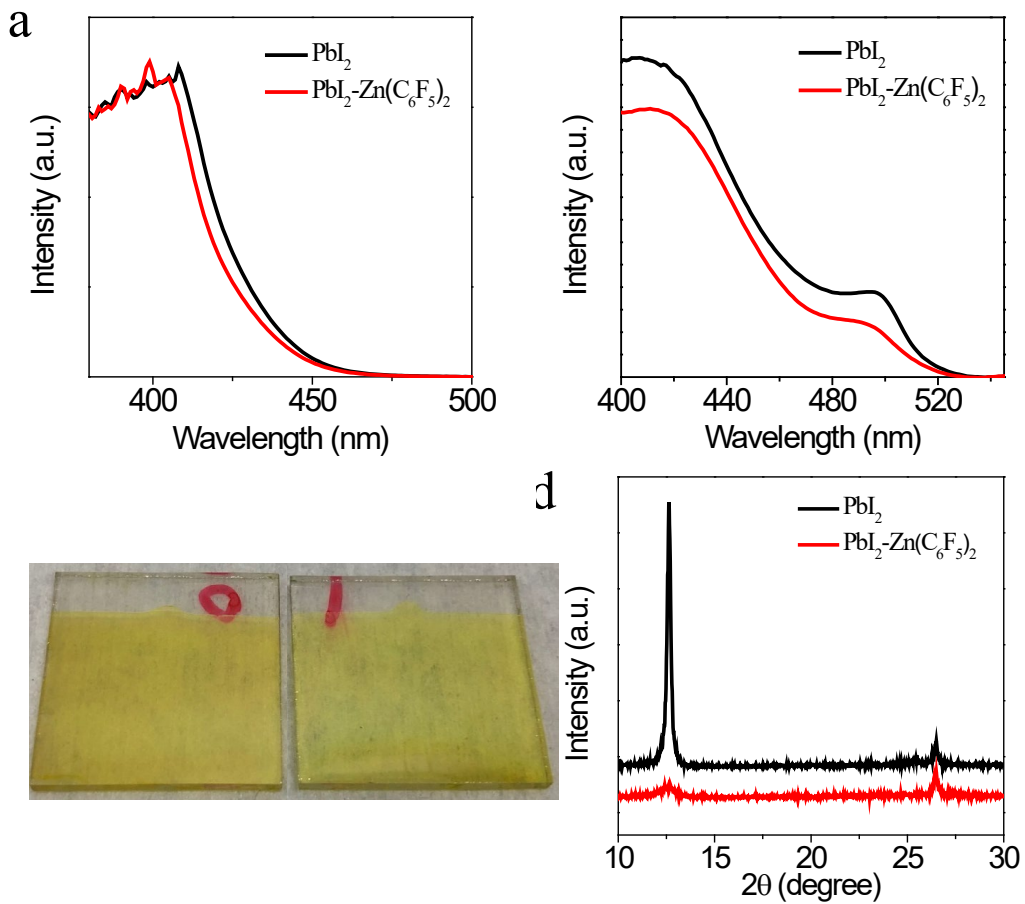


Figure S6. (a) Comparison of UV-Vis spectra for PbI_2 and $\text{PbI}_2\text{-Zn}(\text{C}_6\text{F}_5)_2$ solutions (DMF). (b) Comparison of UV-Vis spectra for PbI_2 and $\text{PbI}_2\text{-Zn}(\text{C}_6\text{F}_5)_2$ films. (c) Images of PbI_2 and $\text{PbI}_2\text{-Zn}(\text{C}_6\text{F}_5)_2$ films. (d) Comparison of XRD for PbI_2 and $\text{PbI}_2\text{-Zn}(\text{C}_6\text{F}_5)_2$ films.

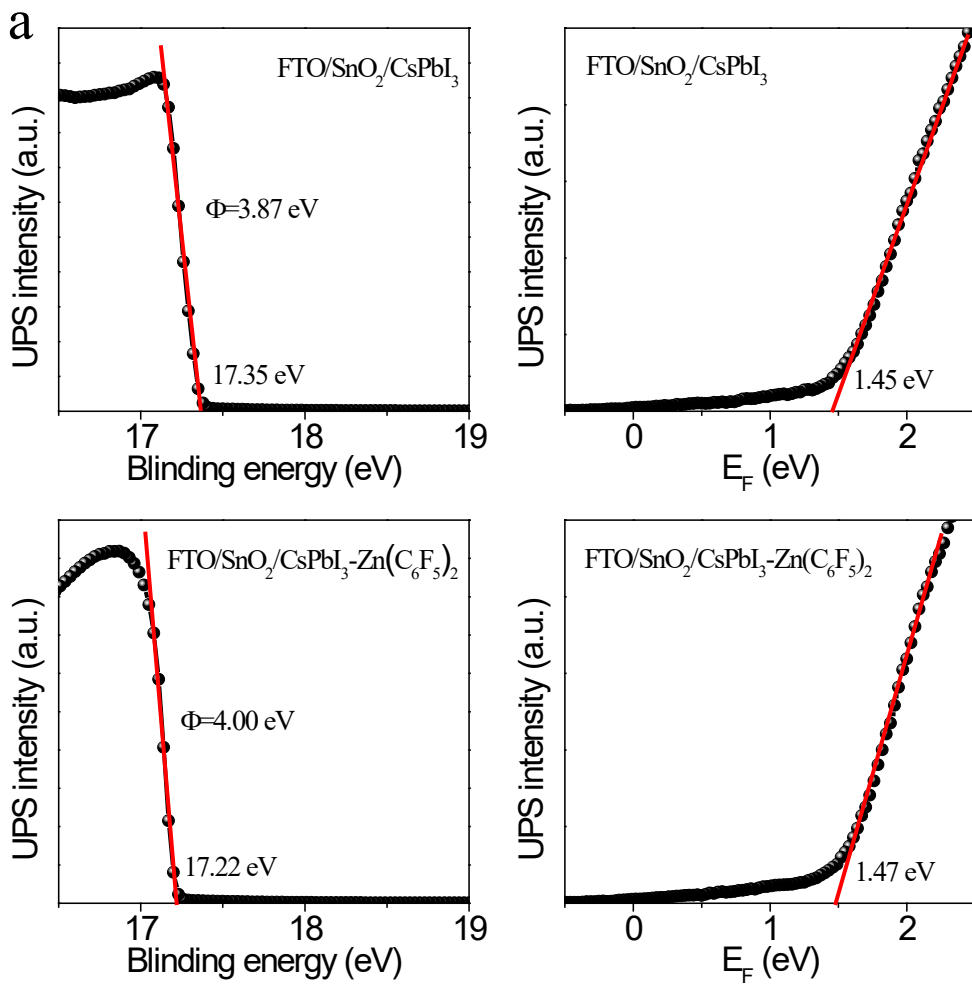


Figure S7. UPS spectra (He-I with photon energy of 21.22 eV) of the CsPbI_3 and $\text{CsPbI}_3-\text{Zn}(\text{C}_6\text{F}_5)_2$ perovskite films deposited on FTO/SnO_2 .

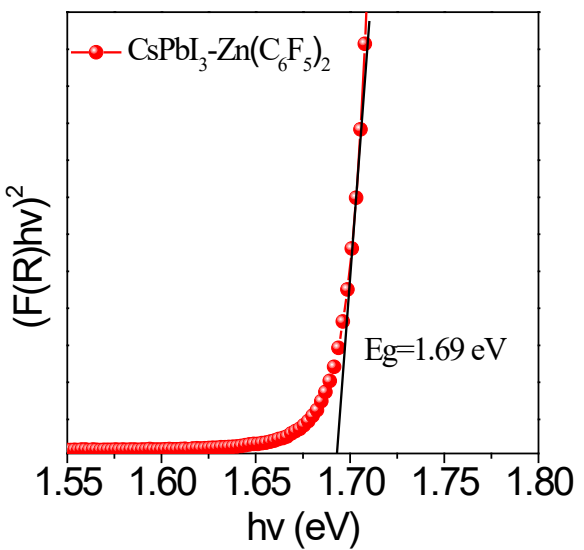


Figure S8. Tauc plot of $\text{CsPbI}_3\text{-Zn}(\text{C}_6\text{F}_5)_2$ assuming a direct band gap.

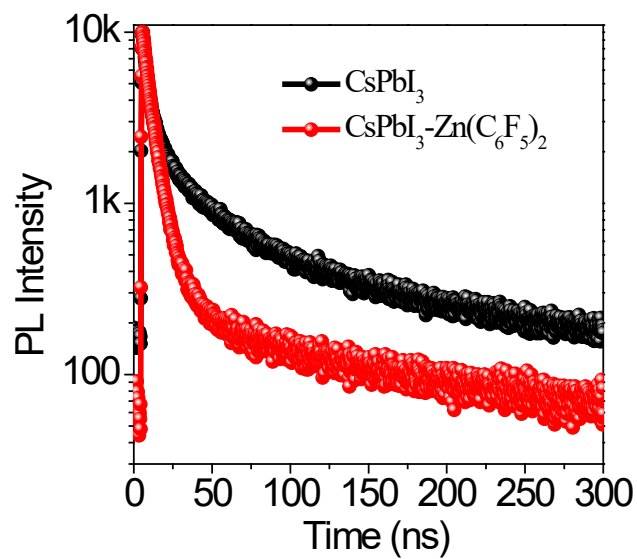


Figure S9. Time-resolved photoluminescence (TRPL) of perovskite layer deposited on SnO_2 .

Table S1. The TRPL statistics of perovskite layer deposited on glass.

Sample	τ_1 (ns)	τ_2 (ns)	$\tau_{ave.1}$ (ns)	$\tau_{ave.2}$ (ns)
CsPbI ₃	14.3	1.1	3.9	1.4
CsPbI ₃ -Zn(C ₆ F ₅) ₂	58.41	8.1	37.6	16.3

References

- [1] J. P. Perdew, Y. Wang, *Phys. Rev. B* **1992**, *45*, 13244.
- [2] P. E. Blöchl, *Phys. Rev. B* **1994**, *50*, 17953.
- [3] P. Giannozzi, S. Baroni, N. Bonini, M. Calandra, R. Car, C. Cavazzoni, D. Ceresoli, G. L. Chiarotti, M. Cococcioni, I. Dabo, *J. Phys.: Condens. Matter.* **2009**, *21*, 395502.
- [4] S. Grimme, *J. Comp. Chem.* **2006**, *27*, 1787.
- [5] K. Momma, F. Izumi, *J. Appl. Cryst.* **2011**, *44*, 1272.